

PAPER • OPEN ACCESS

Enhanced laser absorption from radiation pressure in intense laser plasma interactions

To cite this article: F Dollar *et al* 2017 *New J. Phys.* **19** 063014

View the [article online](#) for updates and enhancements.

Related content

- [Review of laser-driven ion sources and their applications](#)
Hiroyuki Daido, Mamiko Nishiuchi and Alexander S Pirozhkov
- [Fast ignition with laser-driven proton and ion beams](#)
J.C. Fernández, B.J. Albright, F.N. Beg *et al.*
- [The diagnostics of ultra-short pulse laser-produced plasma](#)
Markus Roth



PAPER

Enhanced laser absorption from radiation pressure in intense laser plasma interactions

OPEN ACCESS

RECEIVED

14 January 2017

REVISED

3 April 2017

ACCEPTED FOR PUBLICATION

27 April 2017


PUBLISHED

6 June 2017

Original content from this work may be used under the terms of the [Creative Commons Attribution 3.0 licence](https://creativecommons.org/licenses/by/4.0/).

Any further distribution of this work must maintain attribution to the author(s) and the title of the work, journal citation and DOI.



F Dollar¹ , C Zulick², A Raymond², V Chvykov², L Willingale^{2,3}, V Yanovsky², A Maksimchuk², A G R Thomas^{2,3} and K Krushelnick²

¹ Department of Physics & Astronomy, University of California, Irvine, CA 92617, United States of America

² Center for Ultrafast Optical Sciences, University of Michigan, Ann Arbor, MI 48108, United States of America

³ Department of Physics, Lancaster University, Bailrigg, Lancaster LA1 4YB, United Kingdom

E-mail: fdollar@uci.edu

Keywords: laser plasma interaction, high energy density, laser physics

Abstract

The reflectivity of a short-pulse laser at intensities of $2 \times 10^{21} \text{ Wcm}^{-2}$ with ultra-high contrast (10^{-15}) on sub-micrometer silicon nitride foils was studied experimentally using varying polarizations and target thicknesses. The reflected intensity and beam quality were found to be relatively constant with respect to intensity for bulk targets. For submicron targets, the measured reflectivity drops substantially without a corresponding increase in transmission, indicating increased conversion of fundamental to other wavelengths and particle heating. Experimental results and trends observed in 3D particle-in-cell simulations emphasize the critical role of ion motion due to radiation pressure on the absorption process. Ion motion during ultra-short pulses enhances the electron heating, which subsequently transfers more energy to the ions.

1. Introduction

Recently, significant advances in peak power and repetition rate have been made in the technology of ultra-short-pulse laser systems (pulse length $< 100 \text{ fs}$) [1, 2]. These lasers enable the investigation of the ‘ultra-relativistic’ regime in plasma physics, in which the laser electric field is far beyond that necessary to accelerate an electron to relativistic velocities (e.g. $I_0 \gg 10^{18} \text{ Wcm}^{-2}$). Laser-solid interactions at these intensities have many interesting applications including laser-driven ion acceleration, extreme ultraviolet and x-ray generation, and neutron generation [3–7].

A laser transfers energy efficiently to electrons in a plasma at the reflection point or ‘critical density’, i.e. the point where the laser frequency ω_0 is equal to the plasma frequency $\omega_p = \sqrt{4\pi e^2 n_e / m_e}$ (where e is the electron charge, n_e is the electron density, and m_e is the mass of the electron). At electron densities below the critical density the plasma is transparent. At ultra-relativistic intensities, the laser imposes a substantial radiation pressure on the plasma and may displace the electrons and ions in the plasma, resulting in ‘hole-boring’ [8]. The electrons respond much faster than the relatively massive ions, so that a thermal or electrostatic restoring force occurs if the electrons are displaced. However, during the laser pulse, energy can be transferred directly to the ions due to the electrostatic restoring force. For sufficiently thin plasmas, the radiation pressure may begin to accelerate the ions uniformly, commonly known as the laser piston or radiation pressure acceleration (RPA) regime [9–12]. Furthermore, at such high intensities the critical density itself changes as the effective mass of the electron increases. The relativistic critical density is simply the critical density multiplied by the Lorentz factor, $\gamma = \frac{1}{\sqrt{1 - (v/c)^2}}$. When a laser pulse is sufficiently intense such that the plasma is opaque for lower intensities, but underdense for this relativistic critical density the plasma is said to become relativistically transparent.

Despite advances in laser technology, there is still substantial difficulty in performing an experiment in this regime. Critically, the density profile of a solid density target when the laser pulse arrives is rarely well characterized or controlled, causing substantial variations in the amount of laser energy absorbed and the number of suprathermal, or ‘hot’ electrons produced [13–15]. This preformed plasma is generated from laser

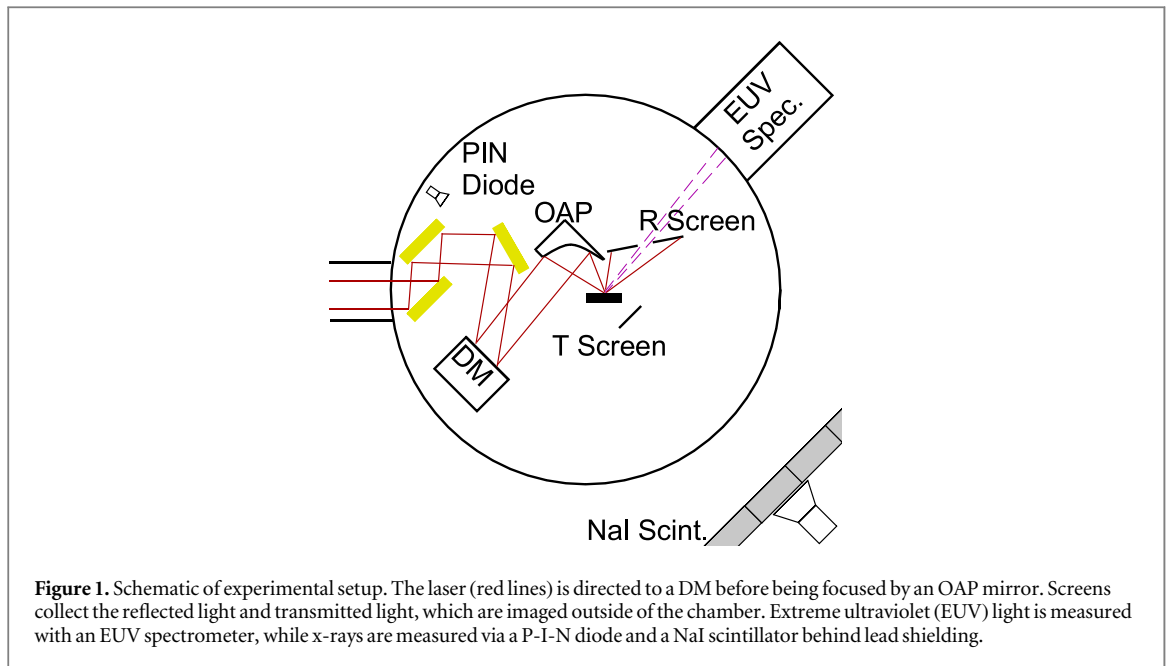


Figure 1. Schematic of experimental setup. The laser (red lines) is directed to a DM before being focused by an OAP mirror. Screens collect the reflected light and transmitted light, which are imaged outside of the chamber. Extreme ultraviolet (EUV) light is measured with an EUV spectrometer, while x-rays are measured via a P-I-N diode and a NaI scintillator behind lead shielding.

prepulses that are difficult to avoid in modern laser systems. The amplified spontaneous emission (ASE) is a nanosecond duration pulse that causes hydrodynamic expansion of the target, resulting in an exponential preplasma density profile that typically extends many wavelengths into the vacuum [16]. For ultrathin targets, this can lower the density substantially, even to the point of being below critical density. The ratio of laser intensity between the main pulse and these prepulses is known as the ‘laser contrast’ ratio. Since the laser focus is typically Gaussian-like, the preplasma profile is not spatially uniform across the focal diameter, which can cause significantly higher laser absorption [17, 18].

It is advantageous to develop scaling laws for laser absorption based on laser intensity or fluence. However, in recent work distinct trends have begun to emerge that suggest that pulse duration is an important parameter that cannot be decoupled from intensity [19, 20]. One reason for this disparity is that the well-established absorption mechanisms such as Brunel or relativistic $\vec{j} \times \vec{B}$ absorption do not account for ion motion [21, 22]. In this article, we isolate dominant absorption mechanisms at ultra-high intensities by varying the incident polarization and the target thickness. Conventional absorption mechanisms are present for thick targets and p polarized incident light, whereas they are suppressed for s polarization. For thin targets where the radiation pressure becomes significant a dramatic increase in absorption occurs. 3D particle-in-cell (PIC) simulations performed highlight the importance of ion motion in the absorption process, where deviations from 1D geometries cause the RPA to direct energy into thermal heating and electron and ion transverse momentum.

2. Experimental setup

The experiments were performed using the HERCULES laser facility at University of Michigan, a Ti:sapphire system ($\lambda = 800$ nm) producing laser pulses with $\tau = 40$ fs duration full-width at half-maximum (FWHM) and an inherent ASE intensity contrast of 10^{-11} [23]. Prior to the experimental chamber, mirrors in a secondary chamber focus the amplified pulse onto a pair of anti-reflection coated BK7 glass substrates that act as plasma mirrors [24, 25]. Each plasma mirror reflects $< 0.15\%$ of s polarized light at 810 nm at low intensities while possessing a measured reflectivity of 65%–70% at high intensity, producing a nanosecond-level ASE contrast of $< 10^{-15}$ [26]. This contrast improvement prevents preplasma formation until 1 ps before the main pulse interaction, so that the density profiles remain extremely sharp ($\sim \lambda/10$). After the plasma mirrors, an *in situ* Mica half-waveplate enables changes to the polarization.

In this experiment, the laser delivered $1.5 (\pm 0.2)$ joules to the target with 55% of the energy in a $1.2 \mu\text{m}$ FWHM focal spot via an $f/1$ off-axis parabolic (OAP) mirror, as shown in figure 1. This results in an on-target intensity of $2 \times 10^{21} \text{ Wcm}^{-2}$ ($a_0 \simeq 30$). A near diffraction limited spot size with a Strehl ratio of 0.6–0.99 was attained by using a deformable mirror (DM, Xinetics).

The targets used in the experiment were free-standing silicon nitride membranes (SiN) with thicknesses of 30–100 nm, $1 \mu\text{m}$ Mylar ($\text{C}_{10}\text{H}_8\text{O}_4$) foils, and polished silicon and fused silica wafers, which will be collectively referred to as ‘bulk.’ These targets possess higher damage threshold than metallic targets, which in turn will further suppress the formation of preplasma. The targets were positioned at the laser focus with an accuracy of

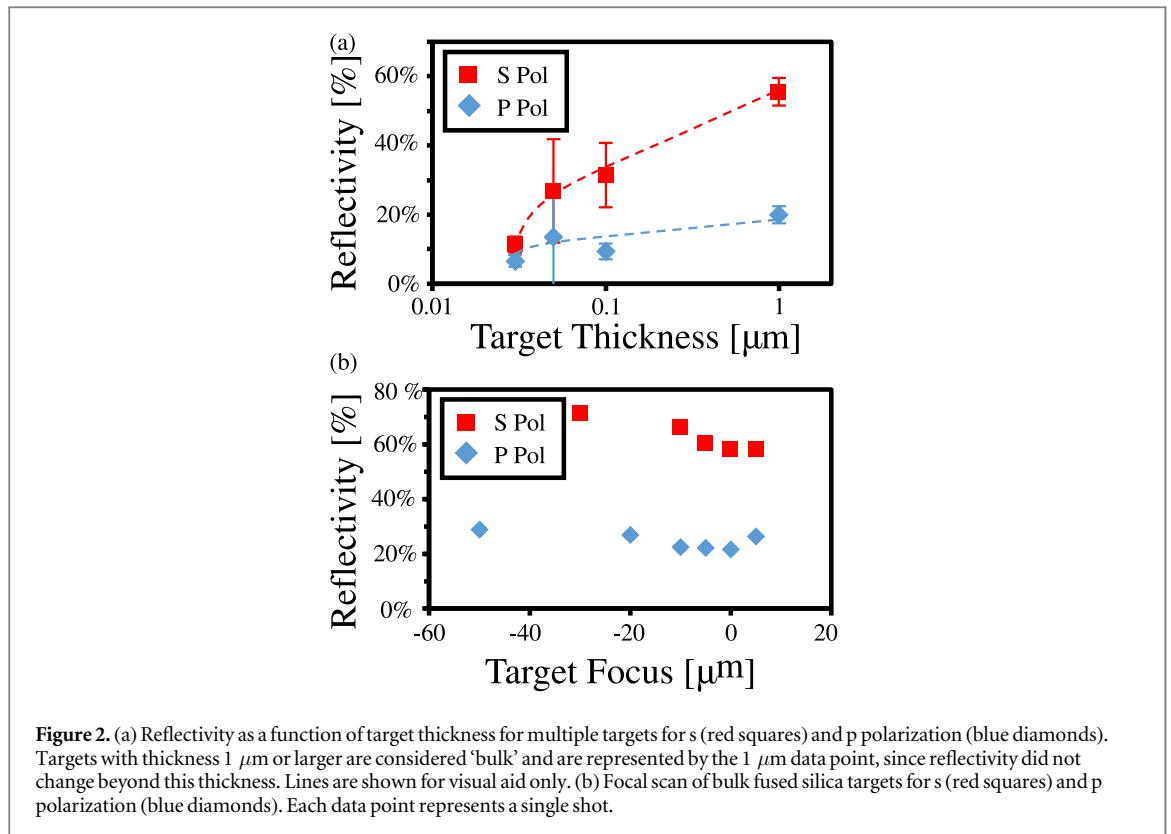


Figure 2. (a) Reflectivity as a function of target thickness for multiple targets for s (red squares) and p polarization (blue diamonds). Targets with thickness 1 μm or larger are considered ‘bulk’ and are represented by the 1 μm data point, since reflectivity did not change beyond this thickness. Lines are shown for visual aid only. (b) Focal scan of bulk fused silica targets for s (red squares) and p polarization (blue diamonds). Each data point represents a single shot.

$\pm 2 \mu\text{m}$ (half of the Rayleigh length) at an incidence angle of 45 degrees. A P-I-N diode with a 25 μm Be Filter and dipole magnet in front measured x-ray emission above 2 keV from the interaction region on the front side of the target. A sodium iodide detector and a plastic scintillator (EJ-204) were used with 10 cm of lead shielding at a position of 2.7 and 9.45 m respectively, to measure high-energy bremsstrahlung radiation from the interaction that arises from suprathermal electrons interacting with solid density material. The yield of both of these x-rays are maximized at the optimal focal position.

Laser light was reflected from the target to a scattering screen positioned 10 cm from the interaction, equivalent to a focal length. This screen was imaged onto a CCD with calibrated neutral density filters and an interference band-pass filter (100 nm $\Delta\lambda$) to examine the reflected 800 nm light. The screen was calibrated with low-energy laser pulses and a calorimeter. A small hole in the screen was present to enable measurement of the EUV emission with an EUV spectrometer [27]. The screen was positioned to collect all detectable specular light. A transmitted light screen was also present in a similar configuration behind the target. An optical imaging spectrometer (Horiba MicroHR) was used to measure the spectrum of the reflected light. The spectrometer shared the same beam path as the CCD to measure energy, using a wedged fused silica beamsplitter to enable simultaneous measurements. For some shots, an infrared filter (Schott Glass BG-39) was added to measure the spectrum of the second harmonic signal.

3. Results

Reflectivity for targets $> 1 \mu\text{m}$ were consistent across materials and are plotted as a single data point in figure 2(a). For the bulk targets, s and p polarized light reflecting $56 \pm 4\%$ and $20 \pm 2\%$ of the fundamental, respectively. P polarized light shows a higher absorption due to Brunel absorption [21] and increased second harmonic generation [28]. Reflectivity was found to be weakly dependent on intensity, with reflectivity for both polarizations increasing by roughly 10% as the target was moved 40 μm out of focus, corresponding to an intensity of $8 \times 10^{17} \text{ Wcm}^{-2}$. The beam profiles for s polarization were clear and sharp and closely resembled the beam at low intensity, as shown in figure 3(a). In the p polarization case, the reflected beam profile showed significant modulation in the amplitude and spatial shape that varied shot to shot. An example profile is shown in figure 3(b). A focal scan was performed with fused silica for both polarizations, and the reflectivities are shown in figure 2(b). This shows the general trend expected from varying the intensity, though defocusing the beam produces a foci, which is highly structured and is shown for qualitative purposes only.

The reflectivity dropped substantially as the target thickness decreased below 100 nm, as shown in figure 2. S polarized reflectivity dropped to $11 \pm 2\%$ for 30 nm targets, while the reflectivity dropped to $7 \pm 2\%$ for p

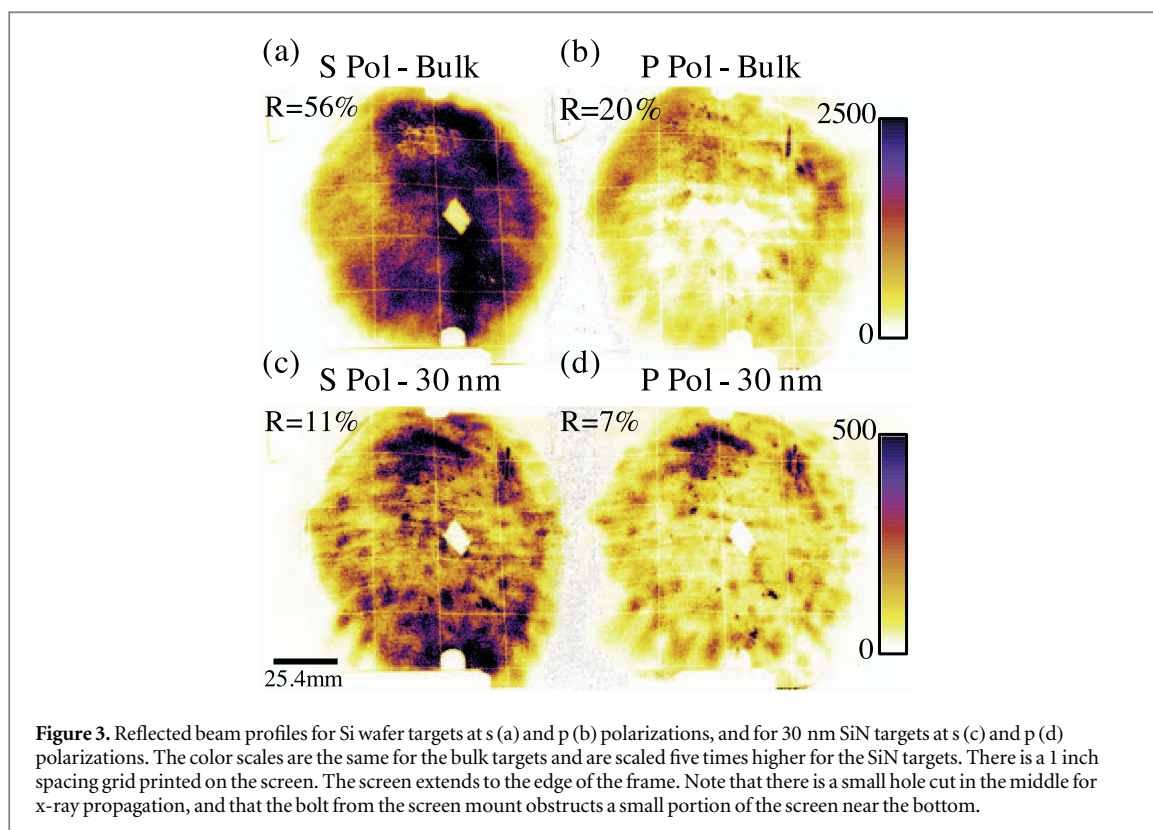


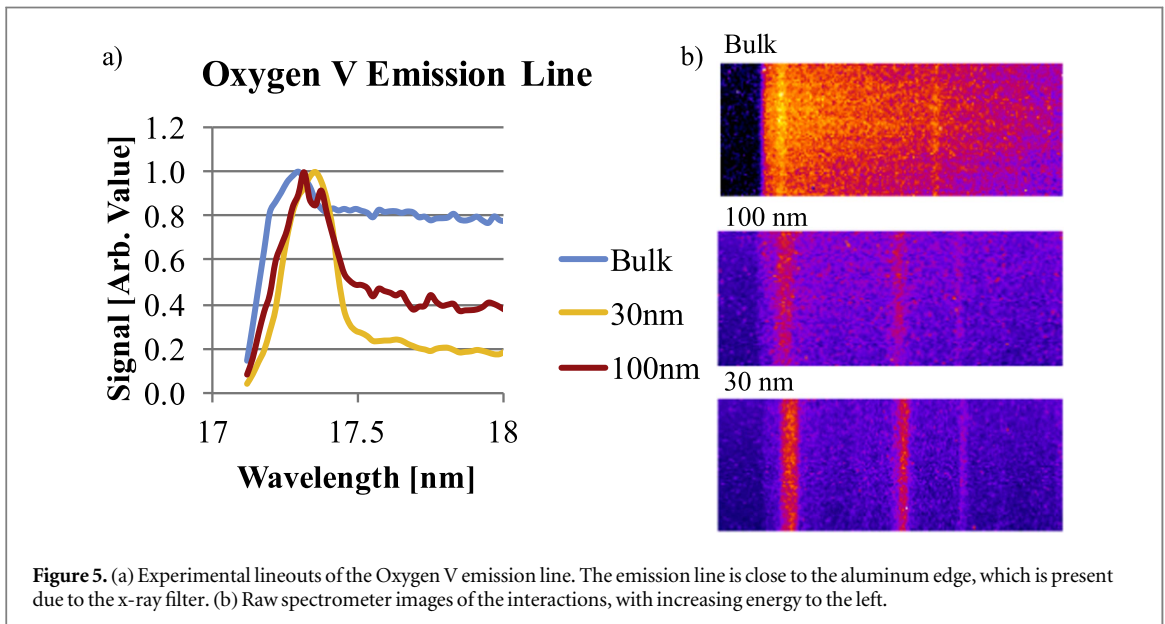
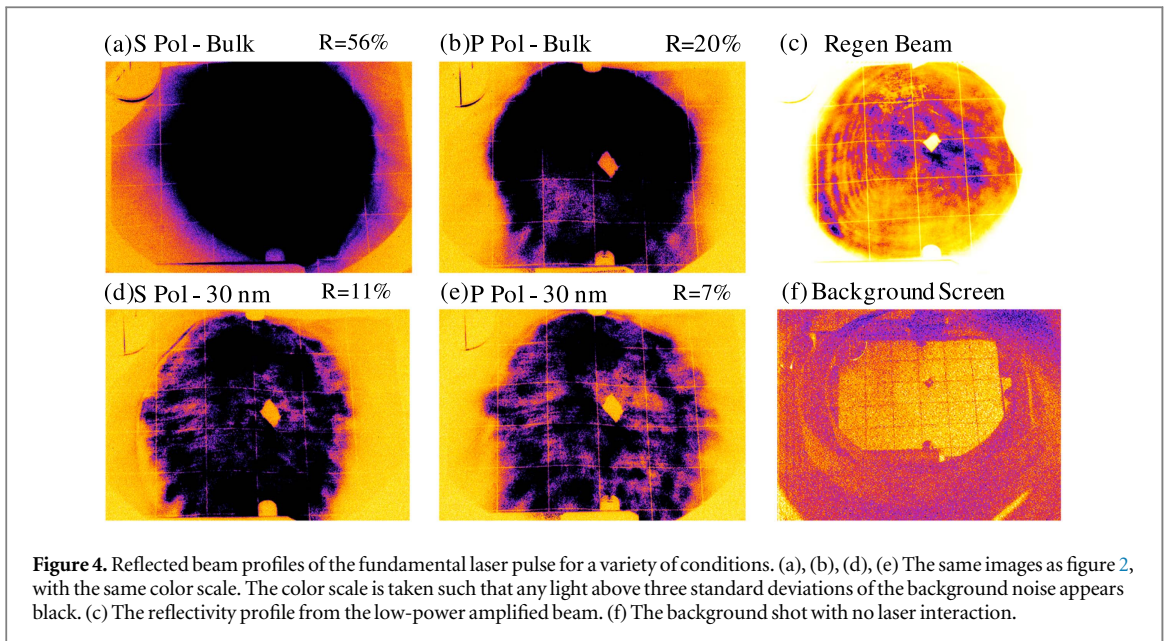
Figure 3. Reflected beam profiles for Si wafer targets at s (a) and p (b) polarizations, and for 30 nm SiN targets at s (c) and p (d) polarizations. The color scales are the same for the bulk targets and are scaled five times higher for the SiN targets. There is a 1 inch spacing grid printed on the screen. The screen extends to the edge of the frame. Note that there is a small hole cut in the middle for x-ray propagation, and that the bolt from the screen mount obstructs a small portion of the screen near the bottom.

polarization. In addition, the beam profile for both polarizations presented with significant modulation that varied shot to shot as shown in figures 3(c) and (d). Although modulated, the beam profiles had a well-defined diameter suggesting that the light is not simply being scattered into a larger cone. No transmitted laser energy was observed within experimental uncertainty ($<5\%$). On the EUV spectrometer, no high harmonic signal was observed for either ultrathin targets or s polarization; and for the ultrathin targets negligible recombination or blackbody continuum was observed. All targets showed comparable signals for the scintillator detectors, though for the ultrathin targets both polarizations generated a signal ≈ 5 times weaker on the PIN diode than for the thicker targets. The optical spectrum was relatively consistent between shots, with blueshifts of up to 7 nm being present for the thin foils. The second harmonic signal was observed for some shots, but poor dynamic range and low signal prevented more quantitative data being reported.

The reflected beam profile screens, being the primary result, are shown again with a different color scale in figure 4. The color scale is chosen such that the hard edge of the beam may be determined. This demonstrates that the reflected light is not simply being sent to a much larger solid angle that overfills the screen. The beams, though clearly modulated, still appear entirely on the screen. Thus, the fundamental light is converted to another form of energy. The unamplified beam is also shown for reference, though it should be noted that in this laser system the unamplified beam is slightly larger than the power amplifier's aperture and exhibits clipping and diffraction rings that are not present in the amplified beam.

The EUV spectrometer used in the experiments is a custom design that enables measurements across a wide spectrum in a single shot. To block lower frequencies from entering the spectrometer and saturating the x-ray CCD (Andor), 800 nm of aluminum was used as an x-ray filter; while simultaneously providing a calibration at the aluminum edge. In a typical interaction, key pieces of information are obtained from the interaction. The hot plasma will emit spectral lines containing temperature and density information. There will be a broad background spectrum that arises from the continuum radiation from the plasma. Finally, high harmonic generation can occur if several conditions are met.

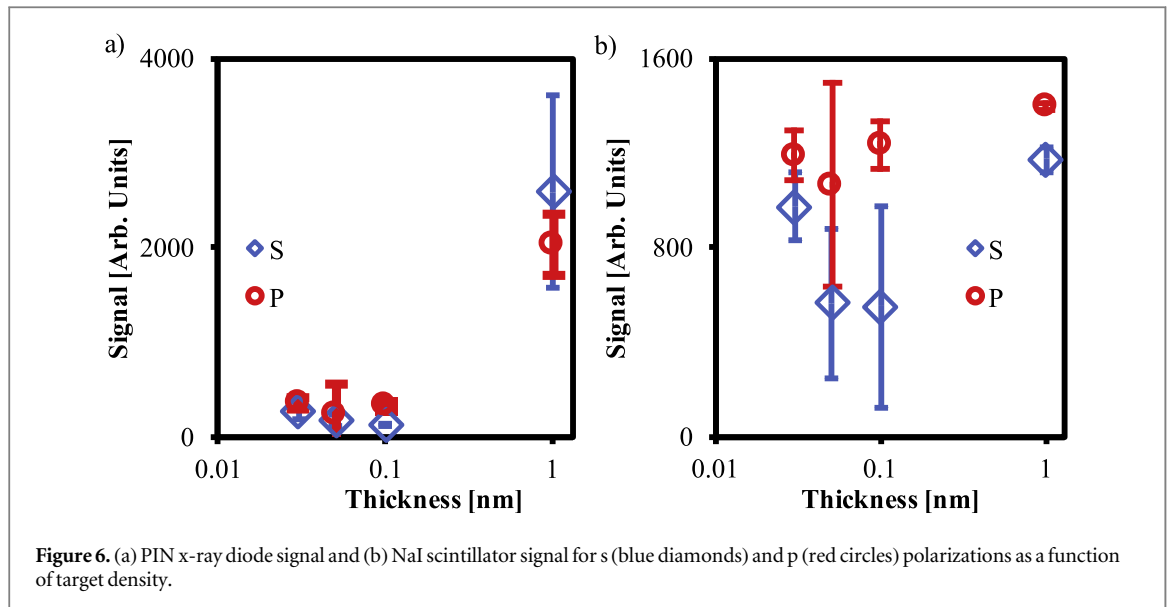
For this experiment, we observe several key features that provide insight into the interaction. Although the blackbody spectrum was suppressed for the ultrathin targets, the Oxygen V emission line at 17.2169 nm was observed to both broaden and redshift (see figure 5). Oxygen is present from hydrocarbons and water vapor that adhere to the surface of any material exposed to air. The thin targets experience radiation pressure acceleration, causing the redshift. There is a large reduction of continuum radiation when thin targets are used (figure 5(b)). Thin targets do not have the dense volume, which enables cold return currents or the interaction of hot plasma in the volume. The hot electrons that are generated at the focus are still produced, and are of sufficient energy such that their effective stopping mechanism is the chamber wall, which will cause Bremsstrahlung radiation,



which is detected by the NaI scintillating detector. Electrons of this energy are sufficiently energetic such that they do not interact strongly with the target, whether it is microns thick or nanometers thick. However, lower-energy electrons will cause x-rays of considerably lower energy, which will interact strongly with the target and generate lower-energy x-rays. Both of these can be observed with the x-ray diagnostics, as shown in figure 6.

4. Relativistically intense absorption for thin foils

At intensities exceeding 10^{16} Wcm^{-2} , the temperature of the plasma rapidly becomes high enough such that collisions during the interaction can be neglected, and thus collisional absorption is neglected in these interactions. In addition, the plasma mirrors prevent the long scale lengths necessary for resonance absorption to be dominant. The remaining high intensity absorption mechanisms include Brunel absorption and relativistic $\vec{j} \times \vec{B}$ absorption, as well as the zero vector potential mechanism [29]. The former two mechanisms describe the transfer of laser energy into electron energy via the electron crossing into a sharp density plasma, where the distinction arises from whether the electron is driven by the laser electric field (Brunel) or the magnetic field ($\vec{j} \times \vec{B}$). For fixed ions, these mechanisms can only exist with p polarized light, as there is no out-of-plane electron motion for s polarized light. The reflectivities for thicker targets are consistent with the lower-intensity studies performed, such as the case for plasma mirrors [24, 30]. Increasing the laser contrast minimizes



preplasma, and in turn minimizes the amount of plasma that exists below the critical density [31]. For very high contrast, scale lengths on the order of tens of nm may be achieved, which is sufficiently thin to suppress high harmonic generation [32–34]. For the bulk targets, the plasma pressure due to the high density is substantial enough such that the ion motion is negligible. Then, the two polarizations of the bulk target represent a comparison between having the absorption mechanisms present and not (p polarization and s polarization, respectively).

In all shots, the reflected light came out in a well-defined profile, where the edge of the beam is well defined (see figure 5). The entirety of the reflected beam lands on the screen, with the exception of the small hole for x-ray transmission. If the reflected power of the s polarized beam on bulk targets is considered, a measurement of the various non-dominant loss mechanisms is extracted. These loss mechanisms include upconversion of laser light into harmonics, resonance absorption not occurring at resonance, and heating of fast electrons. The enhancement of absorption due to the dominant Brunel and $\vec{j} \times \vec{B}$ mechanisms is then simply the difference between the s and p polarizations reflected fundamental for bulk targets.

The reflectivity rapidly decreases with target thickness below 1 μm . This cannot be due to relativistically-induced transparency, since there is no detectable transmission of light. The lack of continuum emission, as well as the weaker signal on the PIN diode clearly demonstrates the reduction of thermal electron bremsstrahlung radiation and return currents in the thin targets (see figure 6). The consistent signal from the scintillator detectors implies that high-energy electrons are still produced at the focus, and previous experiments with similar geometry and targets demonstrated a rise in the maximum ion energy as a function of target thickness [35]. Preplasma scale length does not vary with target thickness, so the same non-dominant mechanisms from the bulk targets should have the same magnitude here. As described more in depth in the following section, the thin targets necessarily include an additional means for laser energy to couple into the plasma, particularly for s polarization. The change of surface reflectivity as a function of thickness requires the plasma conditions change on the timescales of the laser pulse duration.

Oxygen originating from contaminants such as water that adhere to the surface of nearly every target provide a means of determining the motion of the target surface. The observed redshift implies ion motion occurring for the thin targets that is not seen for thicker targets. Although the redshift does not correspond with the same shift in the reflected spectrum, this is not an inherent contradiction as the timescale for plasma emission is on a timescale much longer than that of the interaction. The targets, not being relativistically transparent, are unable to balance the radiation pressure as the thickness decreases. 1D analytical models show that the optimal thickness for RPA is obtained when the foil thickness is $L \approx \frac{a_0 n_{\text{crit}}}{\pi n_e} \lambda$, where $\frac{n_{\text{crit}}}{n_e}$ is the ratio of critical density to electron density. For $a_0 = 30$ at $n_{\text{crit}} = 500$ the optimal thickness is 15 nm [10]. The result is that the measurements of the thin targets show the enhancement of absorption due primarily to the presence of ion motion. Four distinct regimes are present: (1) Dominant Brunel and $\vec{j} \times \vec{B}$ (p polarized bulk), (2) non-dominant losses (s polarized bulk), (3) dominant ion motion (s polarized thin), and (4) Brunel and $\vec{j} \times \vec{B}$ with ion motion (p polarized thin). The reflected beam profile also reveals the presence of low-frequency modulations, indicating that the Rayleigh–Taylor-like mechanism is present in this interaction when ion motion is significant. The instability has been inferred previously from the presence of filamentation in the ion beam and subsequent PIC simulations [36, 37].

When a relativistically intense laser pulse interacts with a solid density plasma, the plasma surface electrons oscillate nonlinearly due to the Lorentz force. Since the motion is locked to the laser pulse, the resultant radiation emission results in harmonic spectra. For higher intensities, the oscillations rapidly accelerate the electrons from rest to the speed of light, and so the effective mass also changes, resulting in a ‘gamma spike’ when the Lorentz factor peaks. The ‘relativistic oscillating mirror’ provides a strong Doppler shift to upconvert the radiation to much higher photon energies. Alternatively, the rapid change in velocity for the electrons from the gamma spikes also provides a model for describing x-ray generation [38]. In these models, the ion surface is assumed to be constant, which provides a well-defined surface to reference for the generation of harmonics.

The influence of lower-order harmonics should be considered for this experiment, since the diagnostics are unable to measure them directly. In recent experiments, it was shown that scaling the intensity for oblique incidence p polarized short-pulse interactions at intensities up to 10^{21} Wcm⁻² could produce a second harmonic signal of $\sim 22\%$ of the main pulse [28]. For targets where the thickness can be considered semi-infinite, even and odd harmonics can be generated from p polarized interactions, while only odd can be generated from s due to the symmetry of the electron oscillations. As mentioned previously, the short-scale length inhibits the generation of higher-order harmonics, but lower orders can still be generated and some portion of the drop in reflectivity in p polarization is likely due to this production. However, these models require an immobile ion population. In the event that the ion front is moving, the point of harmonic generation moves as well, which disrupts the natural phase matching of harmonic production. This is further evidenced by the lack of harmonics for both polarizations for the ultrathin targets, as they undergo ion motion.

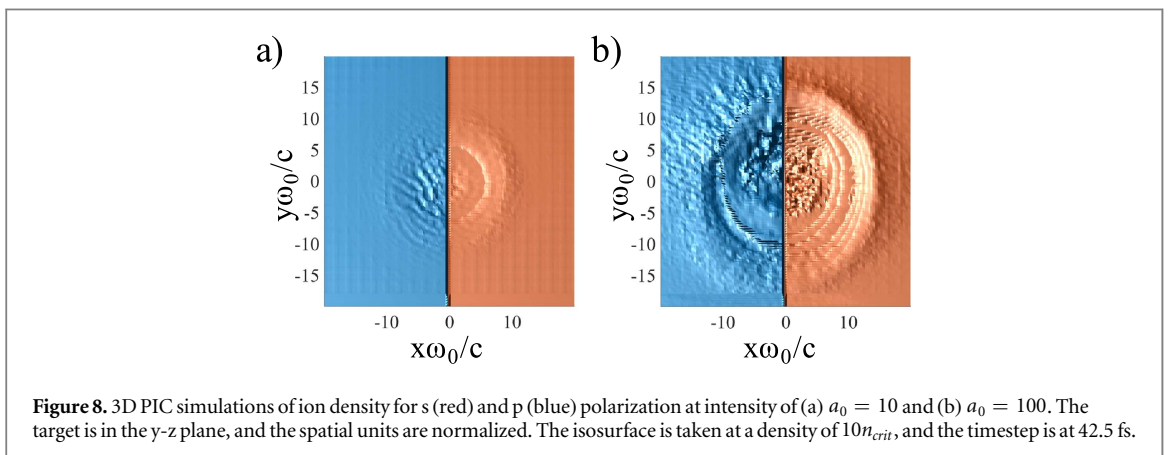
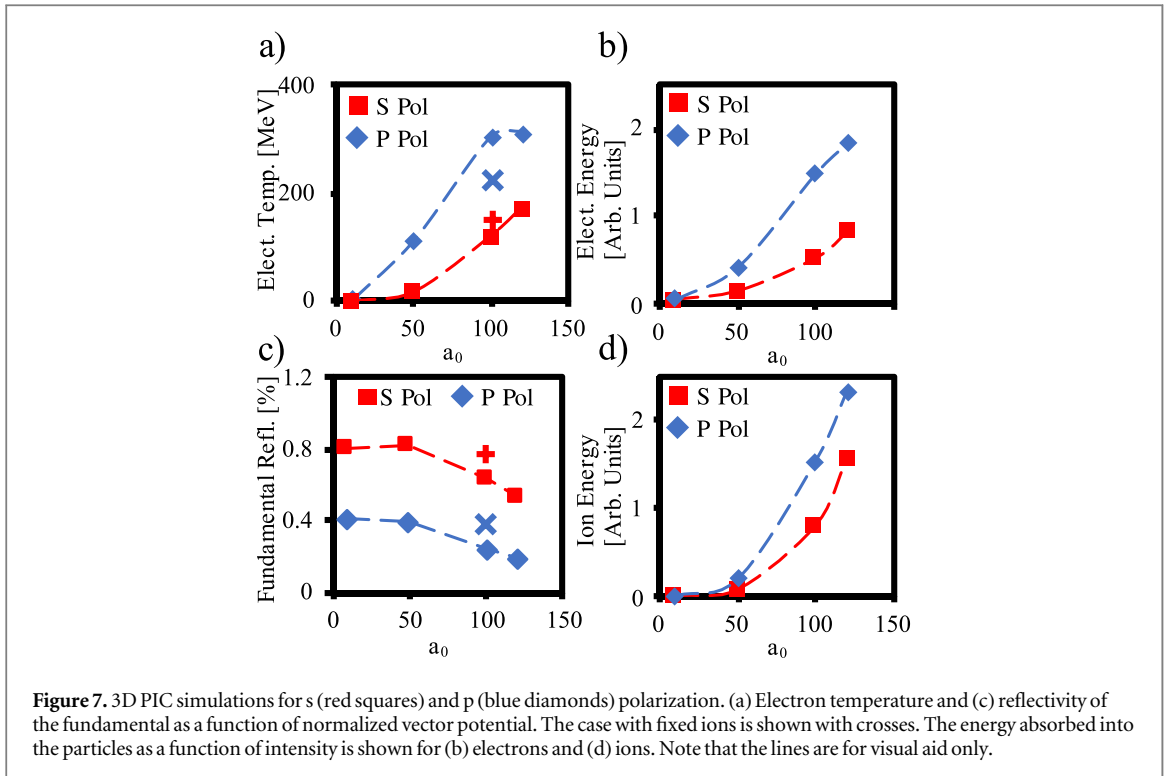
4.1. 3D PIC simulations

3D3P PIC simulations were performed using the OSIRIS code [39], so that further validations can be made. 2D simulations are inadequate for this geometry, as the electron motion due to the laser will be suppressed for s polarization [8]. Due to finite computational resources, the pulse used was 22 fs FWHM, so that the entire pulse could exist in a reasonably sized simulation box. Fully ionized carbon targets with thickness 30 nm and a preplasma scale length of 50 nm were used. The constraints for the simulation box present an issue, as the target thickness cannot be scaled without additional computational resources. To examine the influence of the ion motion, we instead examine the scaling of intensity on a thin foil where low intensity represents the plasma modeling infinitely thick and high intensity represents the regime where radiation pressure is dominant. Because of this variation, the simulations can only provide qualitative results, though conditions have been matched to experimental parameters where appropriate.

Laser intensities varied between $a_0 = 10$ and 120, and were at a 45 degree incidence angle to the target in a 1.2 μm diameter focal spot. The laser pulse shape is a fifth-order polynomial in time and a Gaussian in space, and had both s and p polarization. The cell size was 31.8 nm in each axis, with 64 particles per cell for electrons and 8 particles per cell for ions, and the simulation ran for 65 fs. This is a 3D approach that is similar to the 2D Vlasov simulations done to model deformation with regard to absorption and electron transport [40]. A set of simulations for both polarizations where the ions were immobile was also performed with intensity of $a_0 = 100$. The target was not observed to be underdense during the pulse, nor did the target exhibit relativistic transparency. Keeping the thickness constant also means having a fixed electron areal density, and so the energy imparted to the ions is dependent primarily on intensity [41].

The radiation pressure imparted to the ion motion is a function of the intensity over pulse duration. Since the pulse duration is fixed in these simulations, the intensity itself was scaled to observe the effects of ion motion. Shown in figure 7 are the electron temperature and the reflectivity as a function of intensity. The rapid fall-off with increasing intensity for either polarization demonstrates the enhanced absorption due to the ion motion. For the case of fixed ions, the reflectivity at high intensity is similar to the case for low intensity, though the electron temperature does not show the same relative drop, indicating that the ions themselves are absorbing the laser energy in these intense cases. In addition, as intensity is increased in the simulation, density modulations of the plasma become more extreme, such that at higher intensities the shapes of the surfaces are comparable for both polarizations. The ion-density profile also shows modulation increasing with intensity, particularly with s polarization (figure 8).

Indeed, there are strong modulations present in both polarizations at higher intensities, such that it is difficult to distinguish the two polarizations. Exploring this parameter space will enable the study of very interesting problems. For instance, as intensity increases further relativistic transparency will transfer energy to the rear of the target and mechanisms such as the breakout afterburner can begin to take place [42]. However, the onset of relativistic transparency will occur after considerable heating via radiation pressure, and so the two mechanisms will be in competition. Alternatively, longer pulse durations will enable Rayleigh–Taylor and other fluid instabilities to take place. The simulations presented here show the initial formation of the instability, though both electrons and ions showed filamentation by the end of the pulse, highlighting the role of RPA.



Furthermore, the simulations also show limited center of mass motion of the target at the central focus, suggesting that the reflected beam should not change divergence significantly. Indeed, the Fourier transform of the reflected pulse has a nearly identical divergence, with $< 2\%$ laser energy in a small wing to one side. In addition, the Fourier transform of the reflected fields at $a_0 = 100$ showed a reflectivity of second harmonic signal of 14.3% and 0.65% for p and s polarizations, respectively, in good agreement with prior results [28].

5. Conclusions

Since s polarization inhibits the other absorption mechanisms, radiation pressure is the dominant force that enables energy transfer to the plasma. The thickness dependence is analogous to plasma pressure balance, and limits this absorption to plasmas in which the radiation pressure is comparable to plasma pressure. It is shown that for varying target thickness and polarization, the various dominant absorption mechanisms can be isolated and measured. The drastic change in reflectivity for s polarization shows how strongly the ion motion can affect the interaction, and how much energy can be transferred in even the most ideal situations. We see a steady decrease in the reflected light for s polarization as target thickness decreases, indicating the influence of ion motion. Ultimately, there is little difference between the energy absorbed for ultrathin targets regardless of polarization. This has implications for ion acceleration, where increased energy absorption into electrons forces target normal sheath acceleration rather than RPA, but also for scaling high harmonic generation, since the

surface dynamics and ion motion can alter the properties of the generated x-rays. Careful consideration needs to be given when using fast focusing optics, otherwise the high intensities cannot be exploited in the manner desired.

Acknowledgments

This work was supported by the Department of Energy/NNSA (Grant No. DE-NA0002372), the Army Research Office, and the Air Force Office of Science and Research (Grant No. FA9550-12-1-0310, FA9550-14-1-0282). We acknowledge the OSIRIS consortium (UCLA/IST Portugal) for the use of OSIRIS. Simulations were performed on the Flux Cluster at the University of Michigan and the GreenPlanet cluster at the University of California, Irvine (supported by NSF Grant CHE-0840513).

ORCID

F Dollar  <https://orcid.org/0000-0003-3346-5763>

References

- [1] Yanovsky V et al 2008 *Opt. Express* **16** 2109
- [2] Leemans W et al 2010 *AIP Conf. Proc.* **1299** 3
- [3] Macchi A, Borghesi M and Passoni M 2013 *Rev. Mod. Phys.* **85** 751
- [4] Popmintchev T, Chen M C, Arpin P, Murnane M M and Kapteyn H C 2010 *Nat. Phot.* **4** 822
- [5] Thauray C and Quéré F 2010 *J. Phys. B* **43** 213001
- [6] Zulick C et al 2013 *App. Phys. Lett.* **102** 124101
- [7] Petrov G, Higginson D P, Davis J, Petrova Tz B, McNaney J M, McGuffey C, Qiao B and Beg F N 2012 *Phys. Plasmas* **19** 093106
- [8] Wilks S C, Kruer W L, Tabak M and Langdon A B 1992 *Phys. Rev. Lett.* **69** 1383
- [9] Esirkepov T, Borghesi M, Bulanov S V, Mourou G and Tajima T 2004 *Phys. Rev. Lett.* **92** 175003
- [10] Yan X et al 2008 *Phys. Rev. Lett.* **100** 135003
- [11] Robinson A P L et al 2008 *New J. Phys.* **10** 013021
- [12] Macchi A et al 2010 *New J. Phys.* **12** 045013
- [13] Fedosejevs R, Ottmann R, Sigel R, Kühnle G, Szatmari S and Schäfer F P 1990 *Phys. Rev. Lett.* **64** 1250
- [14] Santala M I K et al 2000 *Phys. Rev. Lett.* **84** 1459
- [15] Mordovanakis A G et al 2009 *Phys. Rev. Lett.* **103** 235001
- [16] Mora P 2003 *Phys. Rev. Lett.* **90** 185002
- [17] Ping Y et al 2008 *Phys. Rev. Lett.* **100** 085004
- [18] Cui Y, Wang W, Sheng Z, Li Y and Zhang J 2013 *Plas. Phys. Cont. Fus.* **55** 085008
- [19] Davies J R 2009 *Plasm. Phys. Cont. Fus.* **51** 014006
- [20] Levy M C, Wilks S C, Tabak M, Libby S B and Baring M G 2014 *Nat. Comm.* **5** 4149
- [21] Brunel F 1987 *Phys. Rev. Lett.* **59** 52
- [22] Kruer W L and Estabrook K 1985 *Phys. Fluids* **28** 430
- [23] Chvykov V, Rousseau P, Reed S, Kalinchenko G and Yanovsky V 2006 *Opt. Lett.* **31** 10
- [24] Dromey B, Kar S, Zepf M and Foster P 2004 *Rev. Sci. Instrum.* **75** 645
- [25] Doumy G, Quéré F, Gobert O, Perdrix M, Martin P, Audebert P, Gauthier J C, Geindre J P and Wittmann T 2004 *Phys. Rev. E* **69** 026402
- [26] Dollar F et al 2013 *Phys. Plasmas* **20** 056703
- [27] Neely D, Damerell A, Parker R and Zepf M 1995 *Central Laser Facility Annual Report RAL-TR-95-025* Technical Report Rutherford Appleton Laboratory pp 113–4
- [28] Streeter M J V et al 2011 *New J. Phys.* **13** 023041
- [29] Baeva T, Gordienko S, Robinson A P L and Norreys P A 2011 *Phys. Plasmas* **18** 056702
- [30] Price D et al 1995 *Phys. Rev. Lett.* **75** 252
- [31] Forslund D W, Kindel J M, Lee K, Lindman E L and Morse R L 1975 *Phys. Rev. A* **11** 679
- [32] Rödel C et al 2012 *Phys. Rev. Lett.* **109** 125002
- [33] Kahaly S et al 2013 *Phys. Rev. Lett.* **110** 175001
- [34] Dollar F et al 2013 *Phys. Rev. Lett.* **110** 175002
- [35] Dollar F et al 2011 *Phys. Rev. Lett.* **107** 065003
- [36] Palmer C A J et al 2012 *Phys. Rev. Lett.* **108** 225002
- [37] Sgattoni A, Sinigardi S, Fedeli L, Pegoraro F and Macchi A 2015 *Phys. Rev. E* **91** 013106
- [38] Baeva T et al 2006 *Phys. Rev. E* **74** 046404
- [39] Fonseca R O et al 2002 *Lect. Notes Comput. Sci.* **2331** 342
- [40] Ruhl H, Macchi A, Mulser P, Cornolti F and Hain S 1999 *Phys. Rev. Lett.* **82** 2095
- [41] Esirkepov T, Yamagiwa M and Tajima T 2006 *Phys. Rev. Lett.* **96** 105001
- [42] Lin Y et al 2006 *Laser Part. Beams* **24** 291